

RESEARCH ARTICLE

Sulci 3D mapping from human cranial endocasts: A powerful tool to study hominin brain evolution

Edwin John de Jager^{1,2}  | Laurent Risser³ | Muriel Mescam⁴ | Caroline Fonta⁴  | Amélie Beaudet^{1,5,6} 

¹Department of Archaeology, University of Cambridge, Cambridge, UK

²Department of Anatomy, Faculty of Health Sciences, University of Pretoria, Pretoria, South Africa

³Institute de Mathématiques de Toulouse, Université de Toulouse, UPS, Toulouse, France

⁴Centre de Recherche Cerveau et Cognition (CerCo), CNRS, Université de Toulouse, UPS, Toulouse, France

⁵School of Geography, Archaeology and Environmental Studies, University of the Witwatersrand, Johannesburg, South Africa

⁶Institut Català de Paleontologia Miquel Crusafont, Universitat Autònoma de Barcelona, Barcelona, Spain

Correspondence

Edwin John de Jager, Department of Archaeology, University of Cambridge, Cambridge, UK.
Email: edwinj.dj@gmail.com

Funding information

South Africa/France (PROTEA) Joint Research Programme, Grant/Award Number: 129923; University of Cambridge Harding Distinguished Postgraduate Scholars Programme

Abstract

Key questions in paleoneurology concern the timing and emergence of derived cerebral features within the human lineage. Endocasts are replicas of the internal table of the bony braincase that are widely used in paleoneurology as a proxy for reconstructing a timeline for hominin brain evolution in the fossil record. The accurate identification of cerebral sulci imprints in endocasts is critical for assessing the topographic extension and structural organisation of cortical regions in fossil hominins. High-resolution imaging techniques combined with established methods based on population-specific brain atlases offer new opportunities for tracking detailed endocranial characteristics. This study provides the first documentation of sulcal pattern imprints from the superolateral surface of the cerebrum using a population-based atlas technique on extant human endocasts. Human crania from the Pretoria Bone Collection (South Africa) were scanned using micro-CT. Endocasts were virtually extracted, and sulci were automatically detected and manually labelled. A density map method was applied to project all the labels onto an averaged endocast to visualise the mean distribution of each identified sulcal imprint. This method allowed for the visualisation of inter-individual variation of sulcal imprints, for example, frontal lobe sulci, correlating with previous brain-MRI studies and for the first time the extensive overlapping of imprints in historically debated areas of the endocast (e.g. occipital lobe). In providing an innovative, non-invasive, observer-independent method to investigate human endocranial structural organisation, our analytical protocol introduces a promising perspective for future research in paleoneurology and for discussing critical hypotheses on the evolution of cognitive abilities among hominins.

KEYWORDS

atlas, density map, human cortex, micro-CT, sulcal pattern, virtual endocasts

This is an open access article under the terms of the [Creative Commons Attribution-NonCommercial-NoDerivs](https://creativecommons.org/licenses/by-nc-nd/4.0/) License, which permits use and distribution in any medium, provided the original work is properly cited, the use is non-commercial and no modifications or adaptations are made.

© 2022 The Authors. *Human Brain Mapping* published by Wiley Periodicals LLC.

1 | INTRODUCTION

Since brains are not preserved in the fossil record, paleoneurologists are presented with the challenge of relying on the imprints preserved on the inner surface of the braincase. These imprints are formed through an intricate balance of tensions and pressures during morphogenesis of the brain and braincase (Moss & Young, 1960). For this reason, researchers make use of endocasts, a moulded cast of the inner surface of the braincase, to extract the negative space originally occupied by the brain and to infer conclusions on brain size, shape, and general surface morphology, such as sulcal patterns and meningeal vascular distribution (Falk, 1980a, 1987, 2014; Holloway, 1978, 2009; Holloway, Broadfield, & Yuan, 2004). In particular, sulcal imprints have been the focus of much interest in paleoneurology (Falk, 2014; Holloway, 1981; Le Gros Clark et al., 1936). Sulci form relatively early during foetal development; the first of which to form is the longitudinal fissure (gestational week: 8–22), separating the two cerebral hemispheres. Primary sulci, namely: the Sylvian fissure, as well as the cingulate-, parieto-occipital- and calcarine sulci (gestational week: 14–16); the central- and superior temporal sulci (gestational week: 20–24); and the superior frontal-, postcentral- and intraparietal sulci (gestational week: 25–26), are responsible for the subdivision of the hemispheres into the frontal, parietal, occipital and temporal lobes, respectively; which were named according to their corresponding bones of the skull. Secondary sulci (gestational week: 30–35) and tertiary sulci (gestational week: 36) follow in development well into the postnatal period, despite volumetric expansion of the brain slowing by the age of 6 years (Stiles & Jernigan, 2010). The intimate morphological relationship existing between the growing brain and the surrounding cranial bones (Moss & Young, 1960) results in these structures being imprinted onto the cranial inner surface very early in one individual's life; these imprints can thus be observed in immature and mature fossil specimens (e.g. Falk, 1980b; Lockwood & Tobias, 1999).

However, these endocasts have limitations. Firstly, information is limited to the external cortical surface, and nothing can be inferred about the subcortical structures (Holloway, Broadfield, & Yuan, 2004). Second, fossil crania are often severely damaged and incomplete or distorted due to taphonomic processes (Beaudet & Gilissen, 2018; Neubauer, 2014). Other limitations reported are related to the presence of intracranial components (e.g. arterial supply of the brain, cerebrospinal fluid, and meningeal membranes) that may blur cerebral details on the endocranial surface (Neubauer, 2014). That being said, Dumoncel et al. (2021) recently reported that there is a good correlation between the endocast (CT) and the brain (MRI), of the same individual, when considering shape and sulcal patterns of the frontal lobes, temporal lobes, occipital lobes and inferior portion of the parietal lobes. They further reported that organisations and morphology of the superior part of the brain are questionable (Dumoncel et al., 2021). Most of the uncertainties in human paleoneurology have resulted from these limitations, which have contributed to long-standing debates. For example, the identification of the lunate sulcus in the endocast of the Taung child (*Australopithecus africanus*; Falk, 1980b; Holloway, 1981). In this context, it may be tempting to

suggest that correct interpretation of details on the endocranial surface almost always relies on the neuroanatomical knowledge of the researcher (Zollikofer & De León, 2013). An additional, less explored (albeit no less important) factor that may bias our interpretations of the fossil record is intra-specific sulcal pattern variation.

Owing to the early works of Connolly (1950), researchers were able to study the extensive sulcal variations of the human brain. Brain atlases that followed, such as those by Ono et al. (1990) as well as Duvernoy and Bourgouin (1999), provided further evidence of the variation of the extant human sulcal pattern. The integration of medical imaging techniques into neurosciences opened new perspectives on how to quantify this variation. In particular, the substantial intra-specific variability in extant human brains has long been a challenge for neurosurgeons when trying to delineate cortical features during keyhole surgery (Ribas, 2010). To solve this problem, researchers have created population-specific brain atlases (e.g. BrainVISA; published by Rivière et al., 2009) that provide a method for data from multiple subjects and modalities to be compared and analysed (Toga et al., 2006). These atlases retain information pertaining to intrapopulation brain variations, proving useful in the detection of pathology in patients and assistive in functional image analysis (Thompson et al., 2000; Toga & Thompson, 2001), and furthermore, revealing previously unreported fascinating aspects of the human brain (Glasser et al., 2016).

Toga and Thompson (2001) described three methods that form the foundation of population-based atlases. First, the popular label-based approach (also known as statistical/probabilistic anatomy maps) involves large volumes of brain data (cortical structures) being manually segmented after the data set is aligned in a stereotaxic space. Second, the deformation-based approach, (based on a warping algorithm), is used to calculate a deformation map of a scan, based on a reference scan optimised by the input atlas; thereby matching cortical structures from one scan to their corresponding structure in another (reference) scan (Bookstein, 1989). In more complex cases, magnitude and directional biases of variations can be determined. Furthermore, assessments of the severity of structural variants outside the normal range can be made to determine if pathology is present. Finally, the density-based approach focuses on producing generalised representations of the anatomy by averaging the intensity of every voxel from multiple 3D images (e.g. MRI) on a voxel-by-voxel basis and aligning the scans into a stereotaxic space to create an average image database (Bookstein, 1989; Evans et al., 1994; Thompson et al., 2000; Thompson & Toga, 1997, 1999; Toga & Thompson, 2001).

Within this context, we propose that a better understanding of the intra-specific variation of the sulcal pattern in extant human endocasts would significantly improve interpretation of the fossil record by avoiding confusion in identifying the imprints. Here we apply the concept of population-based brain atlases, as developed in neuroscience. Specifically, we apply the density-based approach (ideal for aligning images on a voxel-by-voxel basis due to the high interindividual variation inherent to our sample) to characterise the variation of the sulcal pattern imprints in a sample of extant human endocasts. This study ultimately provides a crucial population level reference from which to

guide subsequent analyses of fossil hominin endocasts, with the vision of reducing bias in future sulcal imprint identification endeavours.

2 | MATERIALS AND METHODS

2.1 | Materials

In this paper, we used the sample published in de Jager et al. (2019). This sample includes virtual endocasts extracted from 20 extant human crania with an equal proportion of males and females aged 30–80 years. No pathology affecting the cranial bones was visible. All crania are curated at the Pretoria Bone Collection (see L'Abbé et al., 2005).

2.1.1 | Detection and identification of sulcal imprints

Dry human crania were scanned at the South African Nuclear Energy Corporation (Necsa), Pelindaba, South Africa using micro-focus X-ray tomography (micro-CT; Nikon XTH 225 ST) at a spatial resolution ranging from 94–123 μm^3 (isometric voxel size). Virtual endocasts were generated by using Endex, an automatic segmentation software (Subsol et al., 2010; available at: <https://perso.liris.cnrs.fr/gilles.gesquiere/wiki/doku.php?id=endex>). A semi-automatic detection method was used to automatically identify the sulcal imprints on the surface of the endocasts. The algorithm automatically detects topographical variations, for example, crest lines on meshes to indicate cortical relief in endocasts (Yoshizawa et al., 2007, 2008; available from: <http://www2.riken.jp/brict/Yoshizawa/Research/Crest.html>). By using a custom script (available from: <https://gitlab.com/jeandumoncel/curve-editor>) in Matlab R2013a (Mathworks), detected surface features of interest (e.g. imprints of sulci) were manually identified and labelled by reviewing brain atlases of Connolly (1950) and Ono et al. (1990), and endocast atlases (Beudet et al., 2016, 2019; refer to de Jager et al., 2019 for more details). All unwanted artefacts detected by the algorithm (e.g. imprints formed by meningeal arteries and cranial sutures) were systematically removed.

2.2 | Density maps

2.2.1 | Overview

Here we briefly summarise the approach we developed to compute the anatomical variability of sulcal imprints based on a sample of n endocasts ($n = 20$). We denoted each image of an endocast as E_i , where i depicts values of 1 to n . We first computed a standardised surface of the endocast by using the extracted meshes. Then, we projected all the detected and identified sulcal imprints to this standardised surface. We denoted M_i as the mesh associated with E_i , which specifically represents the endocast. We additionally denoted

C_{ij} as the list of the labelled curves that represent the sulcal imprints on E_i . The index j represents a specific label that corresponds to each sulcal imprint, with $j = 1, \dots, p$. The name of this label was further annotated as L_j . Note that labelled curve C_{ij} may consist of multiple segments.

Finally, the density maps were estimated based on the spatial distribution of the sulcal imprints. This pipeline is summarised in Figure 1, and the different steps are detailed below.

2.2.2 | Average endocast surface

All the meshes representing the endocasts and curve sets representing the sulcal imprints (both in .vtk format) were rigidly aligned and scaled during the extraction and detection process. To calculate the average shape E_{av} of the whole endocast sample set, a void $200 \times 200 \times 200$ voxels 3D image (volume file) $I(M_i)$ was first generated for each mesh M_i . The correspondence between the mesh's (.vtk format) coordinates and the 3D image coordinates was defined so that all meshes were represented as 3D images with a margin of about 10 voxels (10 mm). A value of one was assigned to the voxels in the image corresponding to each node on the corresponding mesh. Thus, the meshes were densely sampled in the 3D images. The resulting 3D images were then smoothed using a Gaussian filter with a standard deviation of five voxels (5 mm). We denote I_{M_i} as the densified and smoothed endocast surface in the future image domain of the average shape A_M .

Once all the 3D images I_{M_i} were computed, their average shape was defined as the barycentre of these images in a specific Riemannian-shaped space following Fiot et al. (2014) and Vialard, Risser, Rueckert, and Holm (2012). A 3D image was randomly picked out of the n images (I_{M_i}) to be the initial guess average image. It was then iteratively deformed towards the Karcher mean (Karcher, 1977), considered (as) the barycentre of the n images (I_{M_i}) in a Riemannian space, of all the images of the entire sample. The main advantage of this method was that it fully preserved the topology of the cranial structures. In practice, this iterative method was performed as follows: We denote $A_{M_{cur}}$ as the estimated average image at the current iteration. At the (very) beginning of the iterative process, $A_{M_{cur}}$ is initiated as being equal to the randomly picked image among the n images (I_{M_i}). Diffeomorphic registration of $A_{M_{cur}}$ on the different images I_{M_i} was then performed using the method of Vialard, Risser, Rueckert, and Cotter (2012), which resulted in n scalar fields encoding the deformation and denoted initial momenta m_i . At each iteration, the current average $A_{M_{cur}}$ is then updated by being deformed using the information in the average momentum $m_{cur} = \text{mean}(m_1, \dots, m_n)$. This process is repeated until $A_{M_{cur}}$ does not present any significant deformation. As shown in Vialard, Risser, Rueckert, and Cotter (2012), this process typically converges after about 5–10 iterations for skulls. Remark that a Karcher mean is defined with respect to a Riemannian Kernel. This kernel models the level of smoothness allowed when moving $A_{M_{cur}}$ to its next estimation. As a consequence, this kernel models the scale at which the average shape A_M is computed. In our

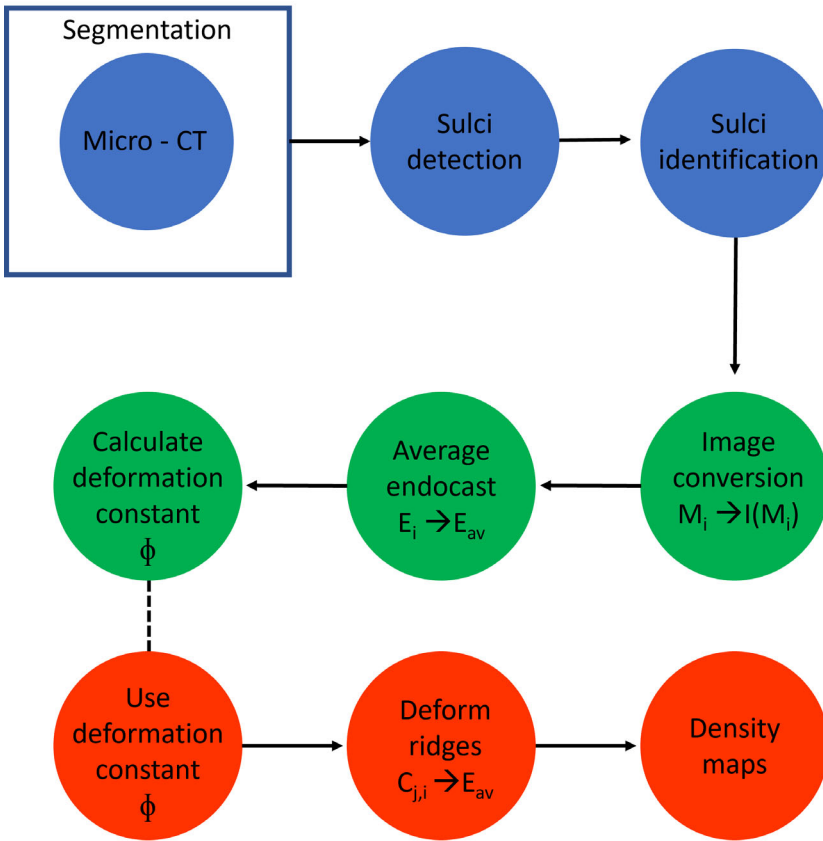


FIGURE 1 Workflow of steps followed to create density maps. Blue: Sulcus detection and labelling procedure; green: Creating average endocast; Orange: Creating density maps for each sulcal imprint

study, we used a Gaussian kernel with a standard deviation of 10 mm. This means comparing shapes having a much larger scale than 10 mm is meaningless (estimations will be unstable), and that the structures having a scale lower than 10 mm are considered as details. We considered this kernel as adapted to compute average endocasts. It however cannot take into account shape details having a size lower than 10 mm. The average shape A_M is finally equal to $A_{M_{cur}}$ at convergence.

2.2.3 | Sulcal imprint variability estimation

Although computing the average image A_M presents a relatively limited interest in itself, it interestingly allows to compute a set of n invertible displacement fields (deformation) ϕ_i which spatially map all features of the E_i to this common template. Each curve set $C_{i,j}$ was then spatially projected at the surface of the averaged endocast using ϕ_i . This projected set was denoted as $P(C_{i,j})$. Considering a specific sulcal label L_j out of all pre-defined labels, all known curves $P(C_{i,j})$ were represented in a single image sampled in the domain of E_{av} (i.e. an image of 200^3 voxels). Note that this image only describes the location of the curves associated with label L_j . We denote I_{C_j} this image. In order to represent the spatial variability of the sulci labelled as L_j on the standardised endocast surfaces, we smoothed each image I_{C_j} with a Gaussian filter with the standard deviation of five voxels (i.e. 5 mm). This smoothing level appeared as a good trade-off between too much smoothing (which would decrease the localisation power of this

method as well as mix information from different sulci) and not enough smoothing for which the density maps would start only representing each individual sulcus. Its intensities were finally normalised so that their sum was one. Each resulting density map I_{C_j} subsequently represented the spatial variability of each observed sulcus. The variations were documented up to two standard deviations.

3 | RESULTS

In general, all sulci ($n = 19$) from the superolateral surface of the brain were identified on 20 endocasts. On average, 73% and 65% of frontal sulci, 42% and 35% of parietal sulci, 88% and 93% of temporal sulci and 51% and 40% of occipital sulci were identified from the left hemispheres (LHs) and right hemispheres (RHs) respectively. Additionally, the Sylvian fissure was clearly identified in almost all endocasts (LHs = 95%; RHs = 85%) (de Jager et al., 2019; Table S1).

The following results of sulcal impressions are listed in a general anterior to posterior order of their appearance on the brain. The impressions of fronto-marginal and fronto-orbital sulci could be seen showing centralised distributions along the caudal margin of the frontal lobe (Figure 2a,b). Similar results can be seen for the superior frontal sulcus, which showed a localised distribution more rostrally along the medial margin of the frontal lobe (Figure 2c). Furthermore, the middle frontal sulcus and the inferior frontal sulcus showed higher variation rates (larger green and blue areas) than the superior frontal

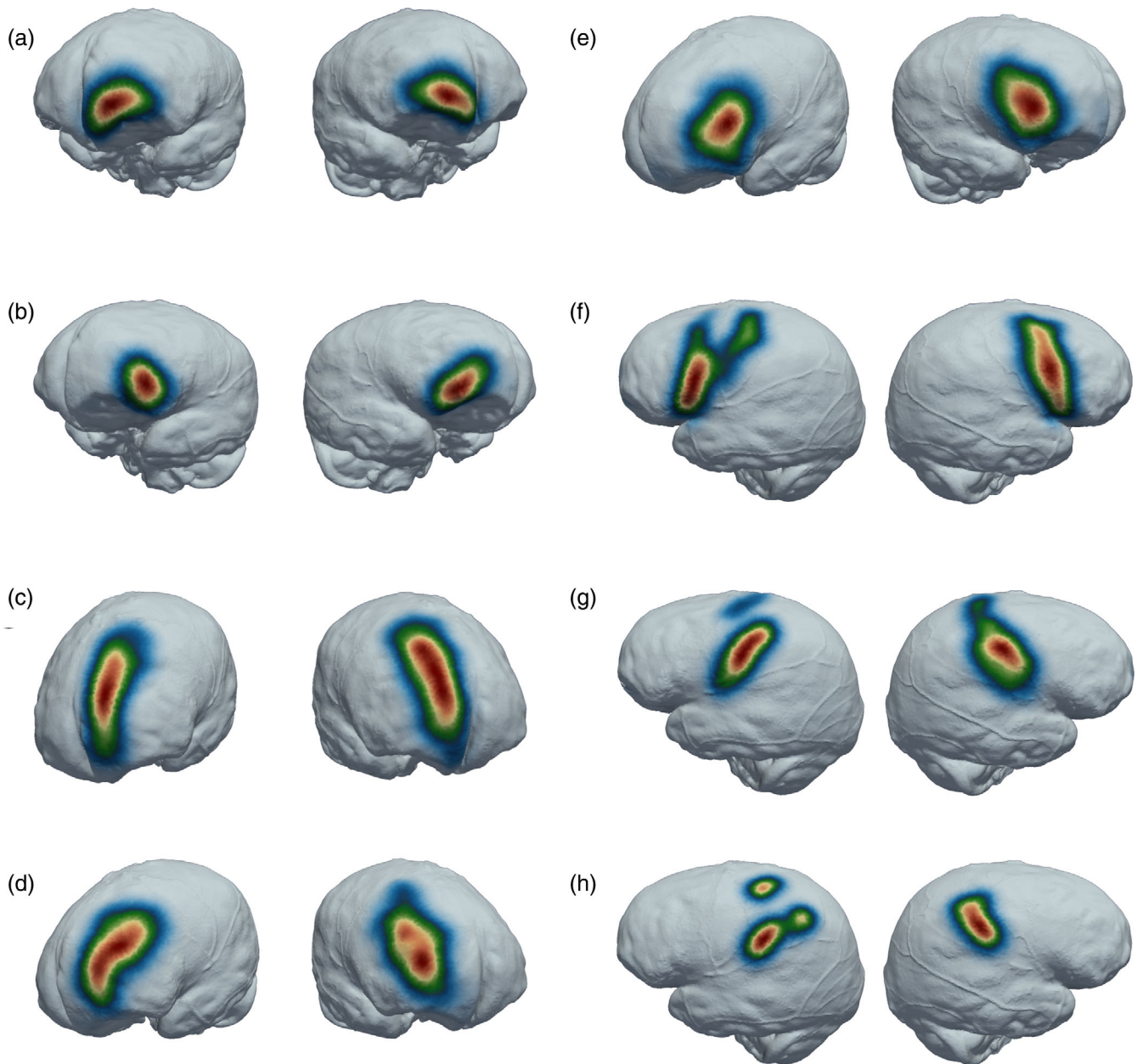


FIGURE 2 Density map indicating the distribution of sulcal imprints around the mean in left and right views. Red indicates the mean distribution and blue indicates mean + 2 standard deviations. (a) Fronto-marginal sulcus; (b) Fronto-orbital sulcus; (c) Superior frontal sulcus; (d) Middle frontal sulcus; (e) Inferior frontal sulcus; (f) Precentral sulcus; (g) Central sulcus; (h) Postcentral sulcus

sulcus (Figure 2d,e). When comparing the distribution between the LHs and the RHs, the superior frontal sulcus shows a more rostrally centred distribution in the LHs compared to the elongated red area on the RHs (Figure 2c). Additionally, the characteristic caudal and rostral centred distribution of the middle frontal sulcus is more prominent on the RHs and more extreme variations, indicated as green on the density maps (Figure 2d).

Scattered distributions were observed for the precentral sulcus, central sulcus, postcentral sulcus, and intraparietal sulcus, particularly on the LHs (Figure 2f,g,h and Figure 3g). The distribution of the right precentral sulcus clearly showed a localised distribution (indicated in

red) along the caudal margin of the frontal lobe and more outliers towards the superior margin of the hemisphere particularly on the LHs. Similarly, the vertically orientated left central sulcus showed a more centralised red distribution located in the middle of the hemisphere just above the temporal lobe, marking the border between the frontal and parietal lobes and more variability towards the superior margin (Figure 2g). The postcentral sulcus showed highly random distributions on the LHs and a clear centralised distribution on the RHs (Figure 2h).

The Sylvian fissure shows a clear horizontal distribution on the lateral surface of the endocast, separating the temporal lobe from the

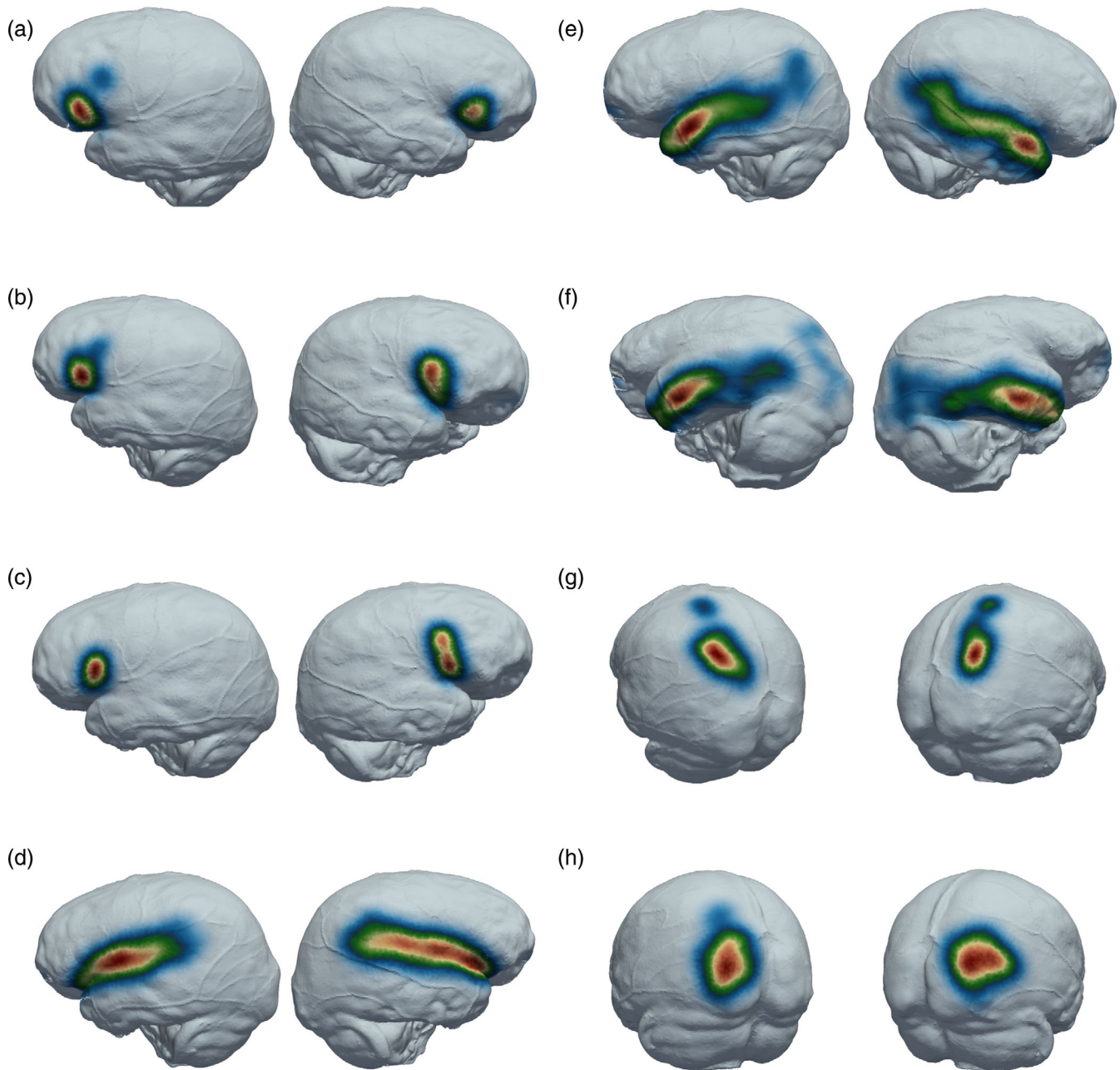


FIGURE 3 Density map indicating the distribution of sulcal imprints around the mean in left and right views. Red indicates the mean distribution and blue indicates mean + 2 standard deviations. (a) Anterior horizontal ramus; (b) Ascending ramus; (c) Diagonal sulcus; (d) Sylvian fissure; (e) Superior temporal sulcus; (f) Inferior temporal sulcus; (g) Intra parietal sulcus; (h) Transverse occipital sulcus

rest of the hemisphere. On the LHs, the Sylvian fissure is centralised (red) rostrally compared to the longitudinal distribution on the RHs (Figure 3d). The anterior horizontal ramus and the ascending ramus of the Sylvian fissure can be seen as centralised (red) distributions on the inferior extremities of the frontal lobe. More extreme variations (blue) of these rami could be seen on the LHs compared to the RHs (Figure 3a,b).

On the temporal lobes, the superior temporal sulcus could be seen directly inferior to the impression of the Sylvian fissure showing a more centralised (red) distribution towards the temporal pole. The

superior temporal sulcus on the LHs showed higher variation rates (blue) towards the parietal lobe (Figure 3e). Similarly, the inferior temporal sulcus could be seen more centralised (red) to the temporal poles with higher variation (blue) towards the occipital lobe on both hemispheres (Figure 3f). Furthermore, the intraparietal sulcus showed two clusters of data; however, the most common area of identification was towards the caudal extremities of the parietal lobe (Figure 3g).

Finally, as for the occipital sulci from most rostral to caudal, the transverse occipital sulcus showed a centralised distribution (red) on the superior lateral extremities of the occipital lobe with more

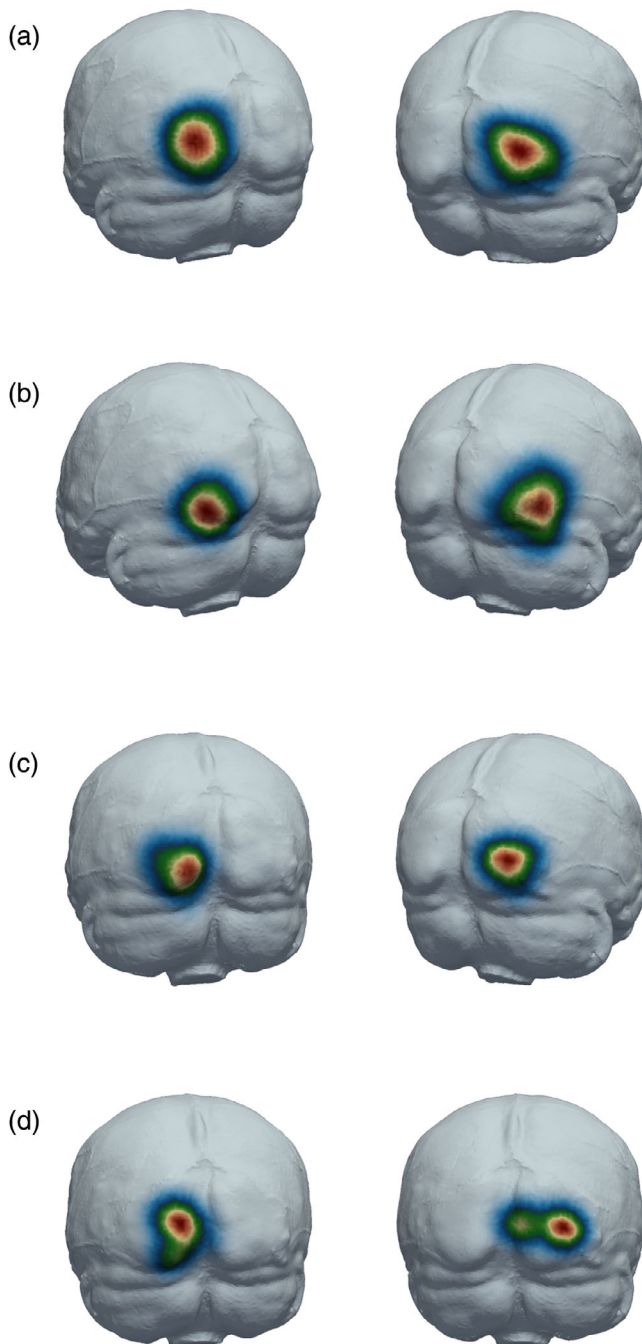


FIGURE 4 Density map indicating the distribution of sulcal imprints around the mean in left and right views. Red indicates the mean distribution and blue indicates mean + 2 standard deviations. (a) Lunate sulcus; (b) Inferior occipital sulcus; (c) Lateral calcarine sulcus; (d) Retro-calcarine sulcus

variation being visible rostral on the LHs (Figure 3h). The lunate sulcus is centralised (red) in the middle of the occipital lobe directly caudal to the impression of the lambdoid suture (Figure 4a). The lateral/inferior occipital sulci showed an obvious distribution close to the inferior-lateral border of the occipital lobes and shows higher variation on the RHs (Figure 4b). Furthermore, the lateral calcarine sulcus and the retro-calcarine sulcus were identified showing distributions on the

posterior extremities of the occipital pole, with variation in the lateral calcarine sulcus stretching laterally on the occipital pole as well as extreme variation seen in the position retro-calcarine sulcus (Figure 4c,d).

The distributions of the major sulci of the frontal lobe overlap in the RHs and in the LHs (Figure 5a). Additionally, overlapping can be observed when viewing the precentral-, central- and postcentral sulci, particularly towards the superior margin on the LHs (Figure 5b). Significant overlapping was observed between the density maps of the anterior horizontal ramus and the ascending ramus of the Sylvian fissure (Figure 5c), and, on the occipital pole, between the distributions of the lunate sulcus, the inferior occipital sulcus, the retro-calcarine sulcus and the lateral calcarine sulcus (Figure 5d).

4 | DISCUSSION

This study provides the first quantitative description of sulcal imprint variation patterns on extant human endocasts. Our method used a density-based approach combined with a user-independent sulcal imprint detection method, implemented on 20 samples. As indicated by the red areas on the density maps, sulcal imprints of the frontal and temporal lobes, and the Sylvian fissure, respectively, could be identified in regions where they are usually found in the brain (Connolly, 1950; Ono et al., 1990). Interestingly, the middle frontal sulcus was most frequently identified as having a rostral- and caudal segment, as described by Connolly (1950) in human brains, and more recently reiterated by Petrides and Pandya (2004) on brain MRIs. The fronto-marginal sulcus was mainly recognised as a horizontally orientated impression, extending laterally from the midline. The fronto-orbital sulcus imprint was observed on the endocasts just anterior to “Broca’s cap”, despite the identification of this sulcus in humans being a rather controversial topic (Connolly, 1950; Falk et al., 2018; Ono et al., 1990; addressed in de Jager et al., 2019). It is evident from the density maps that higher variation can be observed in the anterior horizontal ramus and the ascending ramus of the Sylvian fissure on the LHs, which correlated with findings of asymmetrical variability by Fillard et al. (2007).

High variability in density patterns observed for the precentral, central and postcentral sulcal impressions could result from distortion caused on the endocast by cranial impressions of the middle meningeal vessels, causing missing information (Bruner et al., 2018). Despite the distortion experienced, it is evident from the density maps that the inferior part of the precentral sulcus was reliably identified in most cases, represented by the mean observation in red. The detail with which the regional imprints were detected by our imaging modalities contributed towards our ability to identify the sulcal imprint of interest, thereby reducing the impact of this potential limitation. Similarly, we could not reliably determine the postcentral sulcus, which may be due to the complex branching networks of blood vessels covering this area, and as a result, this feature showed highly variable distribution on the density map. High surface variability of the parietal cortex, housing the postcentral sulcus, was reported on MRI studies (Fillard

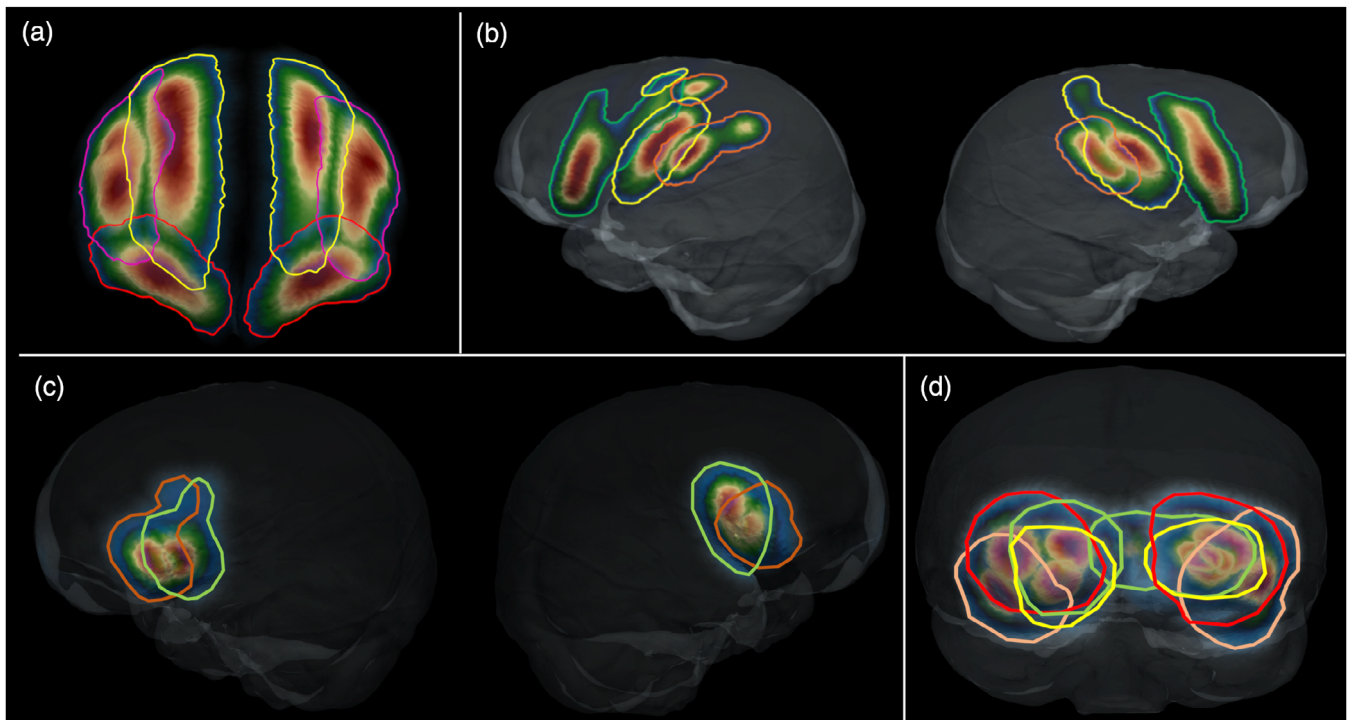


FIGURE 5 Overlap of density maps. (a) Frontal lobe showing the superior frontal sulcus (yellow), middle frontal sulcus (pink) and fronto-marginal sulcus (red); (b) Left and right parietal lobes showing precentral sulcus (green), central sulcus (yellow) and postcentral sulcus (orange); (c) Left and right Broca's area showing anterior horizontal ramus (orange) and ascending ramus (green); (d) Occipital lobe showing the lunate sulcus (red), inferior occipital sulcus (pink), lateral calcarine sulcus (yellow) and retro-calcarine sulcus (green)

et al., 2007; Gómez-Robles et al., 2013). Cerebrospinal fluid (CSF) and blood vessels usually fill the main sulci that delineate functional areas, which, may, subsequently, not be well reproduced on endocasts (Zollikofer & De León, 2013). Although we do not know the handedness of our sample, it is nonetheless clear that the central sulcus on the LHs was more distinctly identified than on RHs, which could be due to the central sulcus more prominently imprinting on the inner surface of the braincase in right-hand dominant individuals, based on findings from Amunts et al. (2000). More research is required to explore this hypothesis.

Based on the distribution seen on the density model, the transverse occipital sulcus can easily be misidentified on the endocasts due to the tendency of the intraparietal sulcus to terminate posteriorly, close to the lambdoid suture (refer to Figure 3). This suture frequently creates phantom markings on the cranial endocast of extant humans and proves helpful in indicating the position of the superior extremities of the parieto-occipital sulcus at the angle formed by the sagittal suture and the lambdoid suture, a landmark often used in neurosurgery (Ribas et al., 2006). Asymmetry was noted when observing the density maps of the lateral calcarine sulcus. This may be due to distortion (created) by the right dominant dural venous sinus groove (García-Tabernero et al., 2018). As addressed by de Jager et al. (2019), age was excluded as a variable in this study due to sample size constraints. Based on Liu et al. (2010) proposal, no new brain expansion occurs in older individuals.

Some of these sulci have been intensely discussed in the fossil record because of their functional role or use as a proxy to indicate

substantial cortical expansion. In particular, because of the link between the Broca's cap and language, the presence or absence of the primitive fronto-orbital sulcus of the human-like horizontal and ascending rami has been the source of essential discussions. Because of the presence of the fronto-orbital sulcus in early hominins (Carlson et al., 2011; Holloway, Broadfield, & Yuan, 2004), it has long been thought that the human-like pattern emerged along with the earliest humans (rev. in Beaudet, 2021). However, a recent revision of the human fossil record rejected this hypothesis, instead suggesting a later emergence of the modern human configuration of the Broca's cap (Ponce de León et al., 2021). Interestingly, our study demonstrates that the distribution of these critical sulci in the Broca's region overlap significantly (Figure 5). As such, we might be cautious when describing this region in the fossil record. The frontal sulci are often described in the fossil record due to the good quality of imprints found in this region of the endocast (e.g. Falk, 2014). The presence and configuration of the middle sulci have been used to identify more derived patterns in the endocasts of early hominins (Falk, 2014). Our maps demonstrate that the positions of the superior and middle sulci are relatively consistent. However, a recent re-analysis of the chimpanzee brain questioned the use of these sulci in evolutionary discussions (Falk et al., 2018). One of the "hottest" debates concerning the identification of sulci in fossil hominins is probably the one surrounding the lunate sulcus. Using fossil specimens from South Africa, scientists have been arguing about a more derived or more ancestral position of this structure for decades (Falk, 1983, 2014; Holloway, 1981;

Holloway, Clarke, & Tobias, 2004). Finding the correct position of the lunate sulcus is of prime interest, since a more posterior (derived) position might indicate a significant expansion of the parietal association cortex. Our results clearly show a substantial overlap of the occipital sulci, including the lunate sulcus, which unequivocally accentuates the risk of mis-identifying this structure in the fossil record. Expanding the atlas to include more samples will likely only improve the robustness of our density maps, which already compare well with direct brain studies (Fillard et al., 2007; Iaria & Petrides, 2007; Juch et al., 2005; Ochiai et al., 2004).

Recent MRI studies on the variability of brain sulci suggest higher variation and asymmetry in sulcal patterns associated with high order association areas (e.g. prefrontal cortex and parietal cortex) and lower variability in sulci delimiting the cerebral lobes such as the Sylvian fissure and the central sulcus (Fillard et al., 2007; Gómez-Robles et al., 2013, 2015). The findings from these authors correlate with our density map data which show higher variability in imprints of the middle frontal sulcus, precentral sulcus, postcentral sulcus, intraparietal sulcus and sulci of the temporal lobe especially the superior- and inferior temporal sulcus on the parietal lobe. In contrary to the above-mentioned studies, our results show less variation on imprints of the Sylvian fissure compared to the imprints of the central sulcus, and our results do not show the unilateral extension of the Sylvian fissure onto the LH's parietal lobe such as the findings of Gómez-Robles et al. (2013). Specifically considering the prefrontal cortex, Juch et al. (2005) reported the origin of superior frontal sulcus to connect to precentral sulcus in at least 74% of their sample, which does not show in our sample due to the lack of imprint formation of the superior part of precentral sulcus. Our data does however show possible overlap between inferior frontal-, precentral- and fronto-orbital sulci which correlates with the variation seen in previous studies on brains (Juch et al., 2005; Ono et al., 1990). Juch et al. (2005) identified frequent juxtaposition of the ascending ramus and precentral sulcus, which correlates with our findings on extant human endocasts. The superior temporal sulcus is known for its segmental patterns (Ochiai et al., 2004), in our findings the imprint of the superior temporal sulcus does not indicate the segmented patterns but instead one prominent imprint distribution starting at the temporal pole and becoming more variable towards the parietal cortex. The opposite can be observed with the imprint of the inferior temporal sulcus which indicates more than one clustering of imprints, correlating with descriptions by Ono et al. (1990), with the most prominent imprint distribution being closer to the temporal pole. Finally, the variation of sulcal imprints on the occipital lobe from our data correlates well with probability maps from brain-MRIs studied by Iaria and Petrides (2007), which similarly reported significant blending between the lunate, the transverse occipital and the lateral occipital sulcus. Similarities of observations made between brains and our results on endocasts support the suggestion that endocasts remain a good proxy for studying sulcal imprint variation.

Our methodological approach provides the first anatomically derived map for sulcal imprint variation on extant human endocasts using an automated sulcal imprint detection method. The detail with

which this method afforded imprint detection will significantly contribute to future studies as it enables the user to virtually interact with a comparative map of extant human sulcal imprints. Furthermore, our model correlates well with sulcal variation previous studies on brains and brain-MRIs, in particular the sulci of the frontal lobes and occipital lobes. This map will consequently prove anatomically invaluable for future studies (and even revisiting previous studies) pertaining to the fossil record. Nevertheless, it is essential to note that cranial endocasts present with significant expanses of missing cortical sulcal information. This is particularly true when studying cortical imprints on extant human endocasts, due to the lack of imprint formation in certain areas which is caused surrounding anatomical structures (e.g. meninges). Furthermore, the sequence of emergence of secondary and tertiary sulci during development of the brain could have effect on the clarity of imprints formed. Fossil samples present the added complication of sulcal imprint detection occasionally being compromised by the poor preservation of these features during fossilisation. Future studies will address this "obstacle" of missing information of cortical imprints, using advanced statistical methods to develop a model that can be used to contribute to the statistical robusticity of our atlas of sulcal imprints.

ACKNOWLEDGMENTS

We thank G. Krüger for collection access; AN van Schoor for anatomical expertise; F. de Beer and L. Bam (Necsa) for data acquisition; J. Dumoncel (AMIS – UMR5288) for technical support. Supported by the South Africa/France (PROTEA) Joint Research Programme (grant number 129923) and by the University of Cambridge Harding Distinguished Postgraduate Scholars Programme; we thank the DST-NRF for sponsoring the Micro-XCT facility at Necsa. Ethical clearance was obtained from the Main Research Ethics committee of the Faculty of Health Science, University of Pretoria August 2017 (No: 339/2017). Additional ethical clearance was obtained from the ethical committee at Cambridge.

CONFLICT OF INTEREST

The authors have no conflict of interest to declare.

DATA AVAILABILITY STATEMENT

The data that support the findings of this study are available from the corresponding author upon reasonable request.

ORCID

Edwin John de Jager  <https://orcid.org/0000-0003-3199-8566>

Caroline Fonta  <https://orcid.org/0000-0001-6326-4044>

Amélie Beaudet  <https://orcid.org/0000-0002-9363-5966>

REFERENCES

- Amunts, K., Jäncke, L., Mohlberg, H., Steinmetz, H., & Zilles, K. (2000). Interhemispheric asymmetry of the human motor cortex related to handedness and gender. *Neuropsychologia*, 38(3), 304–312. [https://doi.org/10.1016/S0028-3932\(99\)00075-5](https://doi.org/10.1016/S0028-3932(99)00075-5)
- Beaudet, A. (2021). The enigmatic origins of the human brain. *Science*, 372(6538), 124–125. <https://doi.org/10.1126/science.abi4661>

- Beaudet, A., Du, A., & Wood, B. (2019). Evolution of the modern human brain. In M. A. Hofman (Ed.), *Progress in brain research* (250th ed., pp. 219–250). Elsevier B.V. <https://doi.org/10.1016/bs.pbr.2019.01.004>
- Beaudet, A., Dumoncel, J., de Beer, F., Durrleman, S., Gilissen, E., Hoffman, J., Oettlé, A., Subsol, G., Thackeray, J. F., & Braga, J. (2016). Morphoarchitectural variation in the extant human endocast. *Journal of Human Evolution*, 101, 65–78.
- Beaudet, A., & Gilissen, E. (2018). Fossil primate Endocasts: Perspectives from advanced imaging techniques. In E. Bruner, N. Ogiyama, & H. Tanebe (Eds.), *Digital endocasts: From skulls to brains* (pp. 47–58). Springer. https://doi.org/10.1007/978-4-431-56582-6_4
- Bookstein, F. L. (1989). Principal warps: Thin-plate splines and the decomposition of deformations. *IEEE Transactions on Pattern Analysis and Machine Intelligence*, 11(6), 567–585. <https://doi.org/10.1109/34.24792>
- Bruner, E., Ogiyama, N., & Tanabe, H. C. (2018). In E. Bruner, N. Ogiyama, & H. C. Tanabe (Eds.), *Digital endocasts: From skulls to brains* (1st ed.). Springer Japan. <https://doi.org/10.1007/978-4-431-56582-6>
- Carlson, K. J., Stout, D., Jashashvili, T., de Ruiter, D. J., Tafforeau, P., Carlson, K., & Berger, L. R. (2011). The Endocast of MH1, *Australopithecus sediba*. *Science*, 333(6048), 1402–1407. <https://doi.org/10.1126/science.1203922>
- Connolly, C. J. (1950). *External morphology of the primate brain*. Charles C. Thomas.
- de Jager, E. J., van Schoor, A. N., Hoffman, J. W., Oettlé, A. C., Fonta, C., Mescam, M., Risser, L., & Beaudet, A. (2019). Sulcal pattern variation in extant human endocasts. *Journal of Anatomy*, 235(4), 803–810. <https://doi.org/10.1111/joa.13030>
- Dumoncel, J., Subsol, G., Durrleman, S., Bertrand, A., Jager, E., Oettlé, A. C., Lockhat, Z., Suleman, F. E., & Beaudet, A. (2021). Are endocasts reliable proxies for brains? A 3D quantitative comparison of the extant human brain and endocast. *Journal of Anatomy*, 238(2), 480–488. <https://doi.org/10.1111/joa.13318>
- Duvernoy, H. M., & Bourgouin, P. (1999). *The human brain: Surface, three-dimensional sectional anatomy with MRI, and blood supply*. Springer Wien.
- Evans, A. C., Collins, D. L., Neelin, P., MacDonald, D., Kamber, M., & Marett, T. S. (1994). Three-dimensional correlative imaging: Applications in human brain mapping. In R. Thatcher, M. Hallet, T. Zeffiro, E. John, & M. Huerta (Eds.), *Functional neuroimaging: Technical foundations* (pp. 145–162). Academic Press.
- Falk, D. (1980a). Comparative study of the Endocranial casts of new and Old World monkeys. In R. L. Ciochon & A. B. Chiarelli (Eds.), *Evolutionary biology of the New World monkeys and continental drift* (pp. 275–292). Springer. https://doi.org/10.1007/978-1-4684-3764-5_13
- Falk, D. (1980b). A reanalysis of the south African australopithecine natural endocasts. *American Journal of Physical Anthropology*, 53(4), 525–539. <https://doi.org/10.1002/ajpa.1330530409>
- Falk, D. (1983). Cerebral cortices of east African early hominids. *Science*, 221(4615), 1072–1074.
- Falk, D. (1987). Hominid paleoneurology. *Annual Review of Anthropology*, 16, 13–30.
- Falk, D. (2014). Interpreting sulci on hominin endocasts: Old hypotheses and new findings. *Frontiers in Human Neuroscience*, 8, 1–11. <https://doi.org/10.3389/fnhum.2014.00134>
- Falk, D., Zollikofer, C. P. E., Ponce De León, M., Semendeferi, K., Alatorre Warren, J. L., & Hopkins, W. D. (2018). Identification of in vivo sulci on the external surface of eight adult chimpanzee brains: Implications for interpreting early hominin Endocasts. *Brain, Behavior and Evolution*, 91(1), 45–58. <https://doi.org/10.1159/000487248>
- Fillard, P., Arsigny, V., Pennec, X., Hayashi, K. M., Thompson, P. M., & Ayache, N. (2007). Measuring brain variability by extrapolating sparse tensor fields measured on sulcal lines. *NeuroImage*, 34(2), 639–650. <https://doi.org/10.1016/j.neuroimage.2006.09.027>
- Fiot, J.-B., Raguét, H., Risser, L., Cohen, L. D., Fripp, J., & Vialard, F. X. (2014). Longitudinal deformation models, spatial regularizations and learning strategies to quantify Alzheimer's disease progression. *NeuroImage: Clinical*, 4, 718–729. <https://doi.org/10.1016/j.nicl.2014.02.002>
- García-Taberner, A., Peña-Melián, A., & Rosas, A. (2018). Primary visual cortex in neandertals as revealed from the occipital remains from the El Sidrón site, with emphasis on the new SD-2300 specimen. *Journal of Anatomy*, 233(1), 33–45. <https://doi.org/10.1111/joa.12812>
- Glasser, M. F., Coalson, T. S., Robinson, E. C., Hacker, C. D., Harwell, J., Yacoub, E., Ugurbil, K., Andersson, J., Beckmann, C. F., Jenkinson, M., Smith, S. M., & Van Essen, D. C. (2016). A multi-modal parcellation of human cerebral cortex. *Nature*, 536(7615), 171–178. <https://doi.org/10.1038/nature18933>
- Gómez-Robles, A., Hopkins, W. D., Schapiro, S. J., & Sherwood, C. C. (2015). Relaxed genetic control of cortical organization in human brains compared with chimpanzees. *Proceedings of the National Academy of Sciences of the United States of America*, 112(48), 14799–14804. <https://doi.org/10.1073/pnas.1512646112>
- Gómez-Robles, A., Hopkins, W. D., & Sherwood, C. C. (2013). Increased morphological asymmetry, evolvability and plasticity in human brain evolution. *Proceedings of the Royal Society B-Biological Sciences*, 280(1761). <https://doi.org/10.1098/rspb.2013.0575>
- Holloway, R. L. (1978). The relevance of Endocasts for studying primate brain evolution. In C. R. Noback (Ed.), *Sensory systems of primates* (pp. 181–200). Springer. https://doi.org/10.1007/978-1-4684-2484-3_8
- Holloway, R. L. (1981). Revisiting the south African Taung australopithecine endocast: The position of the lunatic sulcus as determined by the stereoplotting technique. *American Journal of Physical Anthropology*, 56(1), 43–58. <https://doi.org/10.1002/ajpa.1330560105>
- Holloway, R. L. (2009). Brain fossils: Endocasts. *Encyclopedia of Neuroscience*, 2009, 353–361. <https://doi.org/10.1016/B978-008045046-9.00941-4>
- Holloway, R. L., Broadfield, D. C., & Yuan, M. S. (2004). In J. H. Schwartz & I. Tattersall (Eds.), *The human fossil record* (Vol. 3). John Wiley & Sons, Inc. <https://doi.org/10.1002/0471663573>
- Holloway, R. L., Clarke, R. J., & Tobias, P. V. (2004). Posterior lunatic sulcus in *Australopithecus africanus*: Was it right? *Comptes Rendus Palevol*, 3(4), 287–293. <https://doi.org/10.1016/j.crvp.2003.09.030>
- Iaria, G., & Petrides, M. (2007). Occipital sulci of the human brain: Variability and probability maps. *The Journal of Comparative Neurology*, 501(2), 243–259. <https://doi.org/10.1002/cne.21254>
- Juch, H., Zimine, I., Seghier, M. L., Lazeyras, F., & Fasel, J. H. D. (2005). Anatomical variability of the lateral frontal lobe surface: Implication for intersubject variability in language neuroimaging. *NeuroImage*, 24(2), 504–514. <https://doi.org/10.1016/j.neuroimage.2004.08.037>
- Karcher, H. (1977). Riemannian center of mass and mollifier smoothing. *Communications on Pure and Applied Mathematics*, 30(5), 509–541.
- L'Abbé, E. N., Loots, M., & Meiring, J. H. (2005). The Pretoria bone collection: A modern south African skeletal sample. *Homo*, 56(2), 197–205. <https://doi.org/10.1016/j.jchb.2004.10.004>
- Le Gros Clark, W. E., Cooper, D. M., & Zuckerman, S. (1936). The Endocranial cast of the chimpanzee. *The Journal of the Royal Anthropological Institute of Great Britain and Ireland*, 66, 249–268. <https://doi.org/10.2307/2844081>
- Liu, T., Wen, W., Zhu, W., Trollor, J., Reppermund, S., Crawford, J., Jin, J. S., Luo, S., Brodaty, H., & Sachdev, P. (2010). The effects of age and sex on cortical sulci in the elderly. *NeuroImage*, 51(1), 19–27. <https://doi.org/10.1016/j.neuroimage.2010.02.016>
- Lockwood, C. A., & Tobias, P. V. (1999). A large male hominin cranium from Sterkfontein, South Africa, and the status of *Australopithecus africanus*. *Journal of Human Evolution*, 36(6), 637–685. <https://doi.org/10.1006/jhev.1999.0299>

- Moss, M. L., & Young, R. W. (1960). A functional approach to craniology. *American Journal of Physical Anthropology*, 18(4), 281–292. <https://doi.org/10.1002/ajpa.1330180406>
- Neubauer, S. (2014). Endocasts: Possibilities and limitations for the interpretation of human brain evolution. *Brain, Behavior and Evolution*, 84(2), 117–134. <https://doi.org/10.1159/000365276>
- Ochiai, T., Grimault, S., Scavarda, D., Roch, G., Hori, T., Rivière, D., Mangin, J. F., & Régis, J. (2004). Sulcal pattern and morphology of the superior temporal sulcus. *NeuroImage*, 22(2), 706–719. <https://doi.org/10.1016/j.neuroimage.2004.01.023>
- Ono, H., Kubik, S., & Abernathey, C. (1990). *Atlas of cerebral sulci*. G. Thieme Verlag.
- Petrides, M., & Pandya, D. N. (2004). The Frontal Cortex. In J. Mai & G. Paxinos (Eds.), *The Human Nervous System* (3rd edn., pp. 950–972). Elsevier. <https://doi.org/10.1016/B978-012547626-3/50026-0>
- Ponce de León, M. S., Bienvenu, T., Marom, A., Engel, S., Tafforeau, P., Alatorre Warren, J. L., Lordkipanidze, D., Kurniawan, I., Murti, D. B., Suriyanto, R. A., Koesbardiati, T., & Zollikofer, C. P. E. (2021). The primitive brain of early homo. *Science*, 372(6538), 165–171. <https://doi.org/10.1126/science.aaz0032>
- Ribas, G. C. (2010). The cerebral sulci and gyri. *Neurosurgical Focus*, 28(2), E2. <https://doi.org/10.3171/2009.11.FOCUS09245>
- Ribas, G. C., Yasuda, A., Ribas, E. C., Nishikuni, K., & Rodrigues, A. J. (2006). Surgical anatomy of microneurosurgical Sulcal key points. *Operative Neurosurgery*, 59(4), 177–210. <https://doi.org/10.1227/01.NEU.0000240682.28616.b2>
- Rivière, D., Geffroy, D., Denghien, I., Souedet, N., & Cointepas, Y. (2009). BrainVISA: An extensible software environment for sharing multimodal neuroimaging data and processing tools. *NeuroImage*, 47(1), S163. <https://doi.org/10.1016/S1053-8119>
- Stiles, J., & Jernigan, T. L. (2010). The basics of brain development. *Neuropsychology Review*, 20(4), 327–348. <https://doi.org/10.1007/s11065-010-9148-4>
- Subsol, G., Gesquière, G., Braga, J., & Thackeray, F. (2010). 3D automatic methods to segment virtual endocasts: State of the art and future directions. *American Journal of Physical Anthropology*, 141, 226–227.
- Thompson, P., & Toga, A. W. (1999). Anatomically driven strategies for high-dimensional brain image warping and pathology detection. In W. Toga (Ed.), *Brain warping* (pp. 311–336). Elsevier. <https://doi.org/10.1016/B978-012692535-7/50094-X>
- Thompson, P. M., & Toga, A. W. (1997). Detection, visualization, and animation of abnormal anatomic structure with a deformable probabilistic brain atlas based on random vector field transformations. *Medical Image Analysis*, 1(4), 271–294. [https://doi.org/10.1016/S1361-8415\(97\)85002-5](https://doi.org/10.1016/S1361-8415(97)85002-5)
- Thompson, P. M., Woods, R. P., Mega, M. S., & Toga, A. W. (2000). Mathematical/computational challenges in creating deformable and probabilistic atlases of the human brain. *Human Brain Mapping*, 9(2), 81–92. [https://doi.org/10.1002/\(SICI\)1097-0193\(200002\)9:2<81::AID-HBM3>3.0.CO;2-8](https://doi.org/10.1002/(SICI)1097-0193(200002)9:2<81::AID-HBM3>3.0.CO;2-8)
- Toga, A. W., & Thompson, P. M. (2001). Maps of the brain. *The Anatomical Record*, 265(2), 37–53. <https://doi.org/10.1002/ar.1057>
- Toga, A. W., Thompson, P. M., Mori, S., Amunts, K., & Zilles, K. (2006). Towards multimodal atlases of the human brain. *Nature Reviews Neuroscience*, 7(12), 952–966. <https://doi.org/10.1038/nrn2012>
- Vialard, F.-X., Risser, L., Rueckert, D., & Cotter, C. J. (2012). Diffeomorphic 3D image registration via geodesic shooting using an efficient Adjoint calculation. *International Journal of Computer Vision*, 97(2), 229–241. <https://doi.org/10.1007/s11263-011-0481-8>
- Vialard, F.-X., Risser, L., Rueckert, D., & Holm, D. D. (2012). Diffeomorphic atlas estimation using geodesic shooting on volumetric images. *Annals of the British Machine Vision Association*, 2012(5), 1–12.
- Yoshizawa, S., Belyaev, A., Yokota, H., & Seidel, H. P. (2007). Fast and faithful geometric algorithm for detecting crest lines on meshes. *15th Pacific Conference on Computer Graphics and Applications (PG'07)*, 2, 231–237. <https://doi.org/10.1109/PG.2007.24>
- Yoshizawa, S., Belyaev, A., Yokota, H., & Seidel, H. P. (2008). Fast, robust, and faithful methods for detecting crest lines on meshes. *Computer Aided Geometric Design*, 25(8), 545–560. <https://doi.org/10.1016/j.cagd.2008.06.008>
- Zollikofer, C. P. E., & De León, M. S. P. (2013). Pandora's growing box: Inferring the evolution and development of hominin brains from endocasts. *Evolutionary Anthropology: Issues, News, and Reviews*, 22(1), 20–33. <https://doi.org/10.1002/evan.21333>

SUPPORTING INFORMATION

Additional supporting information may be found in the online version of the article at the publisher's website.

How to cite this article: de Jager, E. J., Risser, L., Mescam, M., Fonta, C., & Beaudet, A. (2022). Sulci 3D mapping from human cranial endocasts: A powerful tool to study hominin brain evolution. *Human Brain Mapping*, 1–11. <https://doi.org/10.1002/hbm.25964>